ELSEVIER

Nuclear Engineering and Design 184 (1998) 163–181

Nuclear Engineering and Design

Quantitative radiography for transient multidimensional, multiphase flows

T.G. Theofanous *, S. Angelini, X. Chen, R. Luo, W.W. Yuen

Center for Risk Studies and Safety, University of California, Santa Barbara, 6740 Cortona Drive, Goleta, CA 93117, USA

Received 28 January 1998; accepted 28 January 1998

Abstract

As computations of transient, multidimensional, multiphase flows are becoming increasingly more realistic, so increases the demand for their detailed experimental validation. The key in this task is the evolution of flow patterns, and the usual approaches of local measurements are inherently limited in meeting this demand. In this paper, we demonstrate the particular suitability of flash X-ray radiography, and the feasibility of reliably quantifying the radiographs of flow regions of various sizes, from microscopic to rather large scale.

1. Introduction

The well-known problems of flow pattern identification and prediction in steady state, one-dimensional, two-phase flows, obtain a whole new dimension in transient, multidimensional, multiphase flows. Here, the pattern is constantly evolving, and the prediction of this evolution is at the heart of the problem. Moreover, in all but certain extreme cases, the concept cannot be reduced to anything more compact than the 'instantaneous and detailed spatial distribution' of the volume fractions of the flow constituents. Recently, multifield theory has come together with computational advances to create an opportunity for the detailed prediction of such flows. A key aspect in such an effort is experimental validation, and a key feature needed in the latter is in being able to capture the 'pattern' (in the sense defined above). In this paper, we are concerned with such measurements, and we take up the use of X-ray attenuation for this purpose.

The technique falls within a broad array, including gamma, beta, and neutron radiations, but as a general rule, quantitative measurements have remained local (i.e. narrow beams), and mostly steady state. Notable exceptions are local void fraction measurements in the works of Smith (1971), who obtained a time resolution of 100 μs using X-rays; Narabayashi et al. (1984), who, also using X-rays, achieved a scanning rate of 200 Hz; and Harvel et al. (1996), who, with 18 X-ray sources and 122 detectors around a 4.5 cm pipe, sampled the cross-sectional void fraction with a resolution of 4 ms. Curiously, the imaging of

* Corresponding author. Tel.: +1 805 8934900; fax: +1 805 8934927; e-mail: theo@theo.ucsb.edu

0029-5493/98/$ - see front matter
PII S0029-5493(98)00195-2

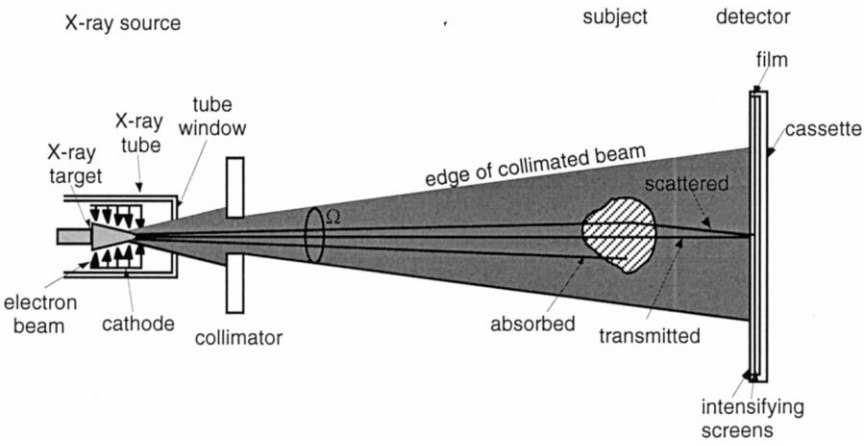

Fig. 1. Illustration of a flash X-ray radiographic arrangement.

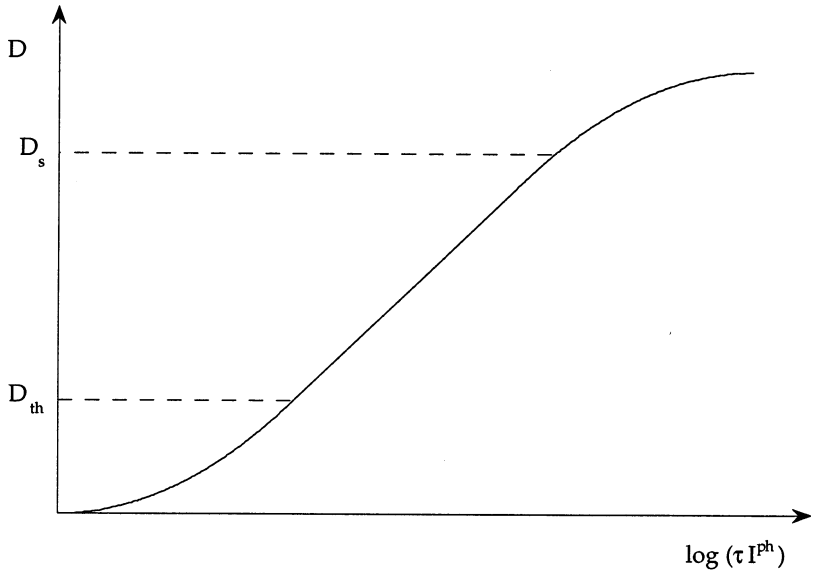

Fig. 2. Characteristic curve relating density and exposure. The useful range is between D_{th} and the saturation level, D_s.

larger regions has remained qualitative, as in the work of Zavaglia and Lindsay (1989) with flash X-rays. Besides the present work, work in quantitative global imaging is also being pursued by Mishima and Hibiki (1997) using neutrons from a nuclear reactor source, with promising results.

The arrangement employed in X-ray radiography is rather straightforward, as illustrated in Fig. 1. Key considerations of the technique, the specific equipment used in this work, and some generic calibration procedures are described in Section 2. Illustrative results from two rather diverse applications are provided in Sections 3 and 4. We conclude with a few summary remarks in Section 5.

2. Measurement principle/procedures

2.1. Attenuation of X-rays and photographic effect

For a planar beam of X-rays, the general atten-

uation law, basically describing photo-electric absorption, can be written as

$$I = I_o e^{-\mu L} \quad (1)$$

where μ is the attenuation coefficient of a material of thickness L, on the path of the X-rays. This attenuation coefficient depends strongly on the material density, and also on the energy of the X-rays, and both of these dependencies can be 'tailored' to meet the requirements of a particular experimental task. Clearly, in multiphase media, discriminating quality improves as conditions are chosen such as to enhance the difference in attenuation coefficients. In particular, this is the case in three-phase, low pressure, liquid-gas systems involving heavy, solid particles, which is our present interest. Here, the particles can be recognized, even when there is significant overlap, between themselves, in the image, and in the remaining portion of the film, the attenuation in the gas (vapor) phase can be neglected. Thus, particle volume fractions can be obtained from geometric consideration, and the gas (vapor) volume fraction, usually referred to as void fraction, can be obtained through the attenuation effected by the liquid. Depending on the particle volume fraction, the former may require more or less sophisticated pattern recognition analysis techniques if necessary, it can even be done by hand, 'clicking' on

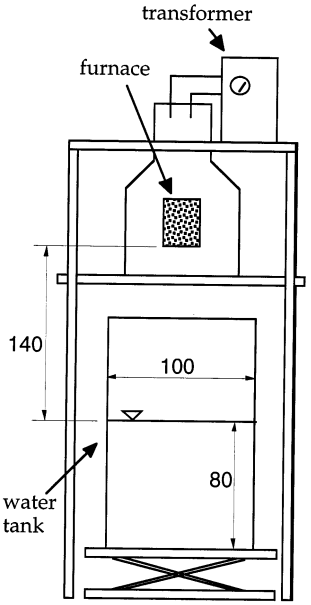

Fig. 3. Schematic of the MAGICO-2000 facility. All dimensions are in cm.

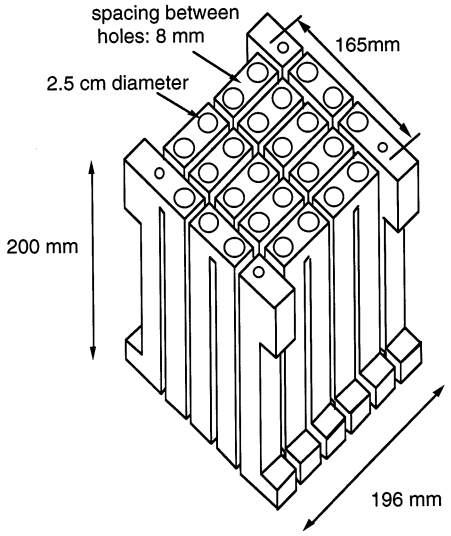

Fig. 4. The heating element in MAGICO-2000.

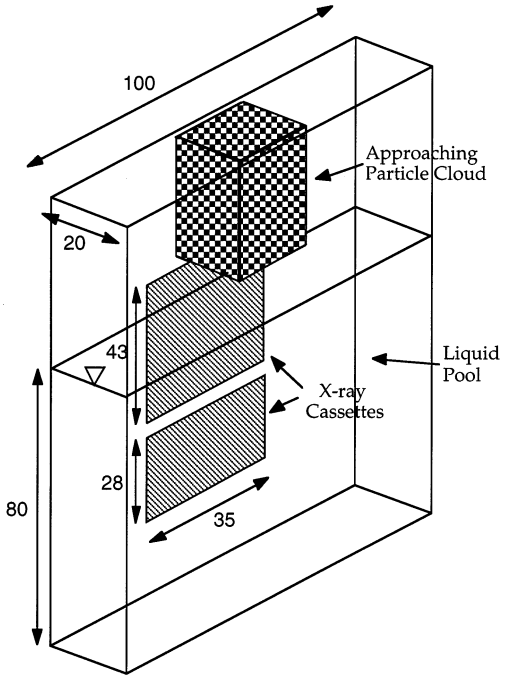

Fig. 5. Interaction tank and positions of X-ray cassettes. All dimensions are in cm.

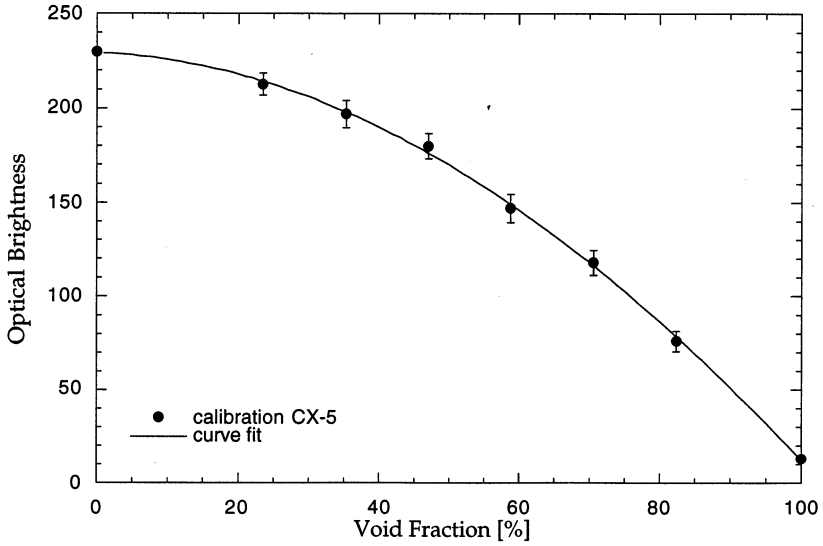

Fig. 6. Sample calibration data and curve fit. Standard deviations also shown.

particles on a computer screen containing the image. For the latter, or the more general case of a two-phase medium where both components attenuate X-rays, an appropriate calibration procedure is necessary. Key considerations are summarized in the following. The discussion is given in terms of photographic film, but it applies analogously to other, technologically more advanced and perhaps more convenient (but also considerably more expensive) approaches for recording the local photon intensity directly, digitally (X-ray sensitive CCD detectors; digital cameras aimed at the intensifying screens).

The key quantity is the density, D, in the developed image; variations in this quantity, across a film, is what allows us to obtain a visual image, and reading of this quantity (using light transmission) is what is needed in quantitative interpretations of such a visual image. More specifically, the density is defined by

$$D = \log \frac{I_{\mathrm{i}}^{\mathrm{l}}}{I_{\mathrm{t}}^{\mathrm{l}}} \tag{2}$$

where $I_{\mathrm{i}}^{\mathrm{l}}$ and $I_{\mathrm{t}}^{\mathrm{l}}$ are the incident and transmitted light intensities, respectively. The 'contrast' is defined as the difference in densities of two points on the film,

$$C_{ij} = D_i - D_j \tag{3}$$

and clearly an increase in contrast is desired to enhance the sensitivity (and hence accuracy) of the measurement. On the other hand, it should also be clear that too great a sensitivity can limit the 'range' of the measurement, through 'saturation.'

To understand the optimization here, we need the relation between density and exposure (Brown, 1966),

$$D = \gamma \log \tau I^{\mathrm{ph}} + A \tag{4}$$

where I^{ph} is the photon intensity (some multiple of the X-rays, as amplified by the intensifying screens used), τ is the exposure time, γ is a characteristic of the film emulsion and processing details, and A is a constant. Now, using Eqs. (2) and (4) in Eq. (3), we get

$$2.3 C_{ij} = \ln \frac{I_{\mathrm{t},j}^{\mathrm{l}}}{I_{\mathrm{t},i}^{\mathrm{l}}} = \gamma \ln \frac{I_i^{\mathrm{ph}}}{I_j^{\mathrm{ph}}} = \gamma\mu(L_j - L_i) \tag{5}$$

which shows how contrast increases both with γ and μ. On the other hand, Eq. (4), plotted in Fig. 2, shows how saturation can limit the range as contrast increases. To optimize is to maximize the sensitivity within the range of interest, and besides the choice of emulsion and developer, development time and temperature affect the results.

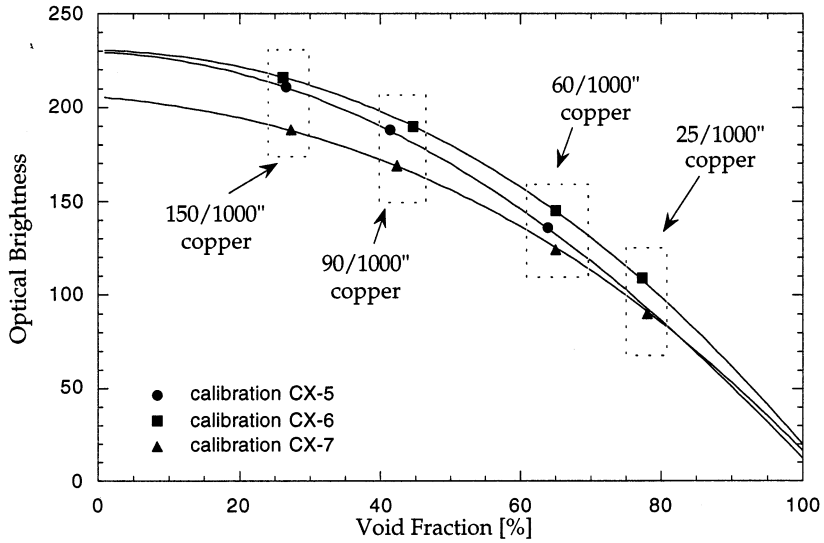

Fig. 7. Calibration curves and witness marks from different radiographs.

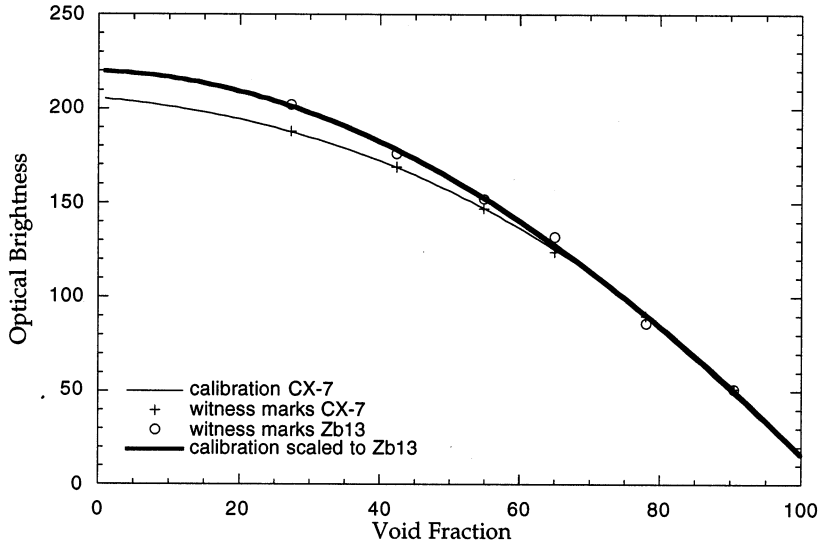

Fig. 8. Use of witness marks to scaling the calibration curve for run Zb13.

Table 1
Conditions for the cold MAGICO-2000 runs in a two-dimensional slab geometry

Run	Particle size (mm)	Total mass (kg)	Particle volume fraction (%)	Impact velocity (m s^{-1})	X-Ray time (s)
ZCN	2	5.5	~6.5	~5.2	0.2, 0.25, 0.3, 0.35, 0.4
ZCT	7	5.0	~0.5	~4.4	0.1, 0.8

Table 2
Conditions for the hot MAGIC0-2000 runs in a two dimensional slab geometry

Run	Particle size (mm)	Total mass (kg)	Volume fraction (%)	Impact velocity (m s^{-1})	Particle temperature (°C)	Water subcooling (°C)	X-Ray time (s)
Z11	2	5.5	4.2	5.2	1550	0	0.3
Z12	2	5.7	4.2	5.2	1400	10	0.3
Zb13	7	4.8	5.5	5.2	1600	0	0.3
ZT14	7	5.1	0.5	4.4	1650	0	0.8
ZT15	7	4.4	0.5	4.4	1800	0	0.8
ZT16	7	2.6	0.5	4.4	2000	0	0.8

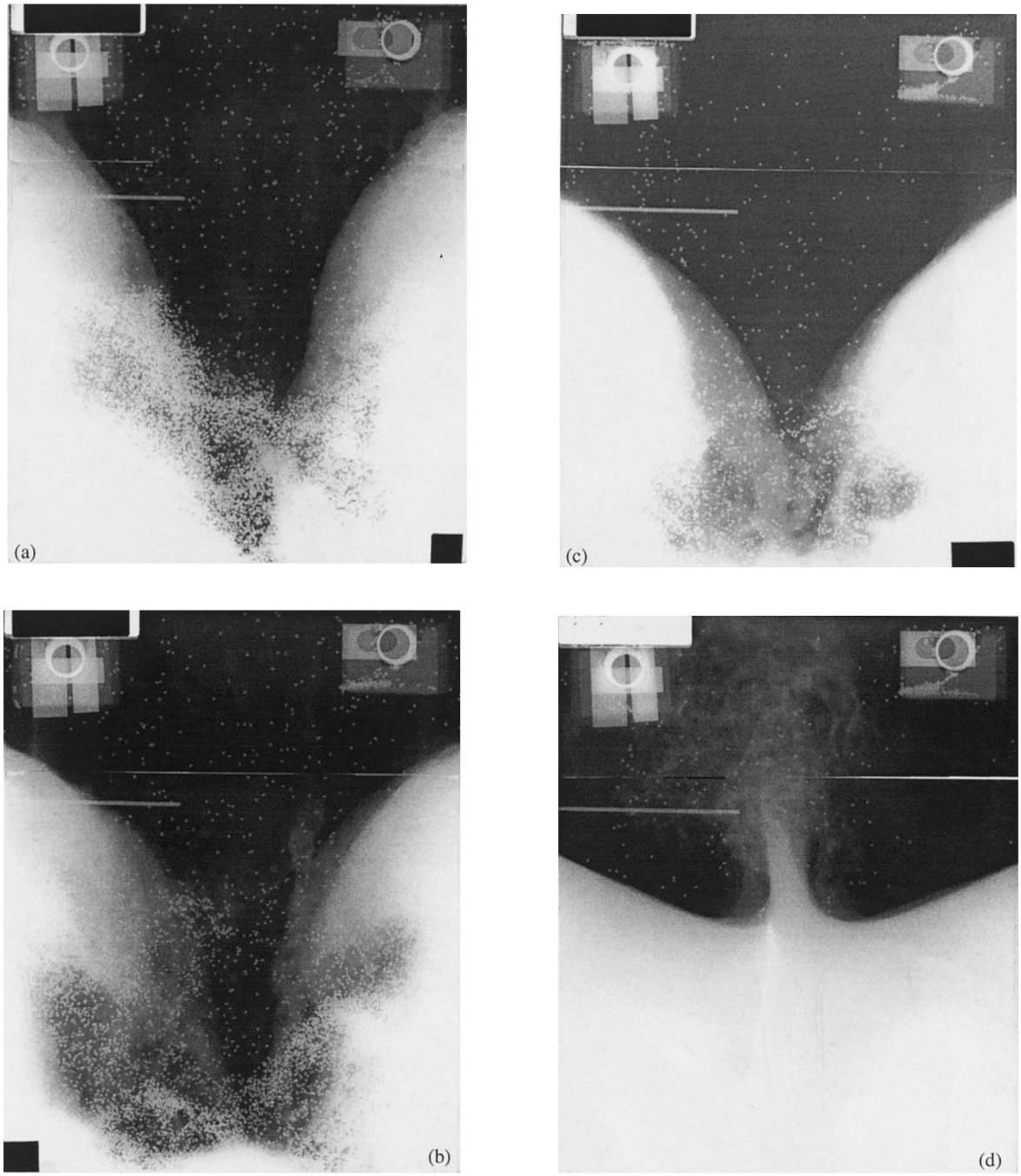

Fig. 9. Radiographs for runs ZCN. The (a), (b), (c) and (d) correspond to times of 0.2, 0.25, 0.3, and 0.4 s, respectively.

Another interesting interplay arises between the contrast and 'sharpness' of the photographic image. From geometric consideration, sharpness requires that the source size and the subject-to-film distance be very small compared to the source-to-subject distance. However, this latter distance is

usually limited by the source strength and the geometric ($1/r^2$) decay of the intensity. Trying to compensate for this by increasing the energy level of the X-rays would decrease the attenuation coefficient and hence also the contrast. Alternatively, since the attenuation coefficient increases for decreasing X-ray energies, low energies maximize the contrast, which further reduces the maximum distance at which the source can be placed.

2.2. Equipment and calibration procedures

The X-ray equipment utilized in the present work is:

- Hewlett–Packard flash X-ray generator, model 43734. Equipped with a soft X-ray tube. Variable X-ray energy capability up to 450 kV. Pulse duration 10^{-7} s.
- Kodak X-ray films, model X-omat AR2.
- Kiran intensifying screens, model Lightning Plus for the MAGICO, and MCI Optonix, model Optex High Plus for the SIGMA.
- Processing is made by hand, under rigorously controlled conditions.
- Radiographs are scanned by a drum scanner, model Iteck 200S, at a resolution of 200 dpi in grayscale. Spatial resolution is 0.13 mm.

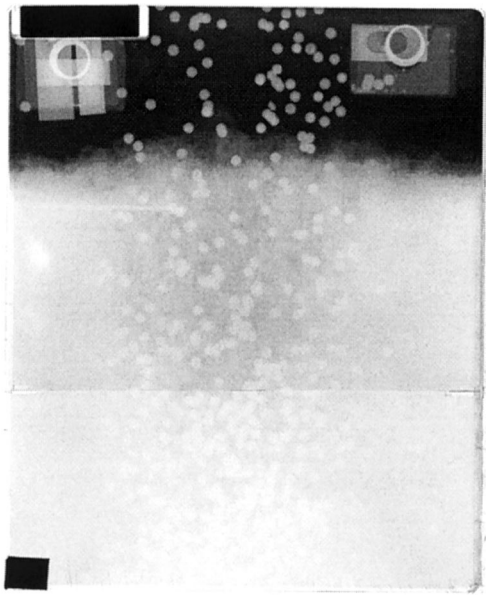

Fig. 10. The mixing zone in run ZCT at 0.8 s.

Local densities on an exposed film can be converted to attenuating material volume fractions, through the use of calibration curves. Particulars for the two cases considered here are given in the next two sections. Here, we provide a general discussion on 'uncertainty.'

Beyond maximizing contrast within the range of interest, and beyond obtaining the calibrations under representative geometries, uncertainties in such measurements principally relate to '**reproducibility**'—from the X-ray shot to the development of the film, and to the scanning process. Even under the best controls, variations arise, and these need to be taken into account. So-called 'witness' pieces are used for this purpose. These pieces, strategically placed so as not to interfere with the subject image, are present in both calibrations and in the actual measurement. By selecting several thicknesses so as to span the degree of attenuation over the region of interest, they allow a determination of the degree of applicability of a calibration curve to any particular exposed film. Moreover, for slight variations, they provide the basis for adjusting the calibration to correct for the variation. As is usually the case with difficult measurements, we found that quality improves with experience, yielding, eventually, quite good control as well as understanding of uncertainty. Typically, relative errors under 10% could be achieved.

3. Application to mixing of hot particle clouds in volatile liquid pools

3.1. The MAGICO facility

The MAGICO facility was designed to deliver kg-quantities of particulates, at temperatures up to 2000°C, into liquid pools of various shapes, dimensions, and saturation levels. The purpose is to study the detailed interactions (collectively called 'multifield aspects') obtained during such transient plunging processes, and to produce a data base appropriate for testing fundamentally-based, CFD predictions. It is of utmost importance, therefore, that initial and boundary

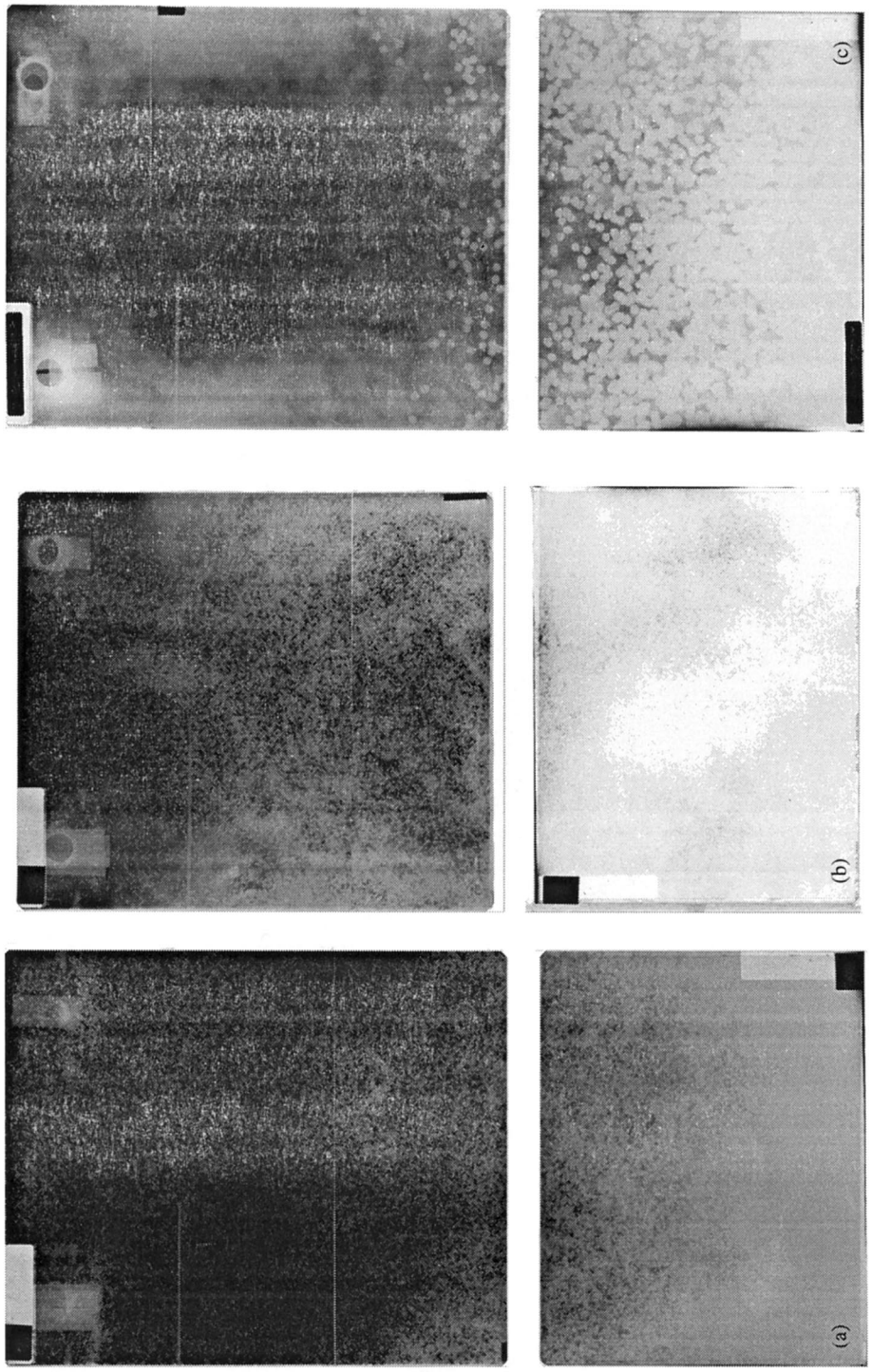

Fig. 11. Radiographs obtained in the runs of Table 2. The (a) through (f) correspond to runs 11 through 16 in the table.

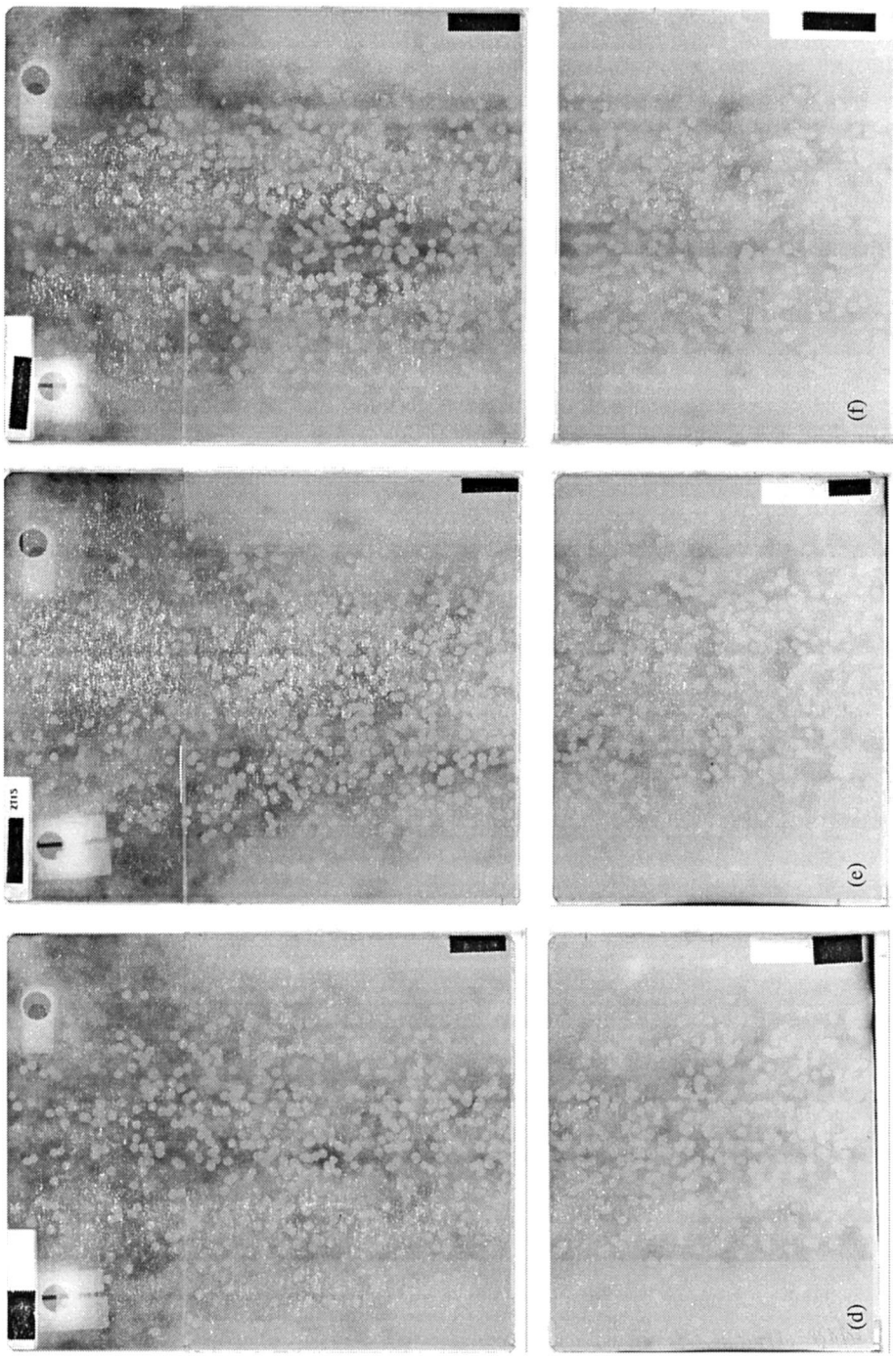

Fig. 11. (*Continued*)

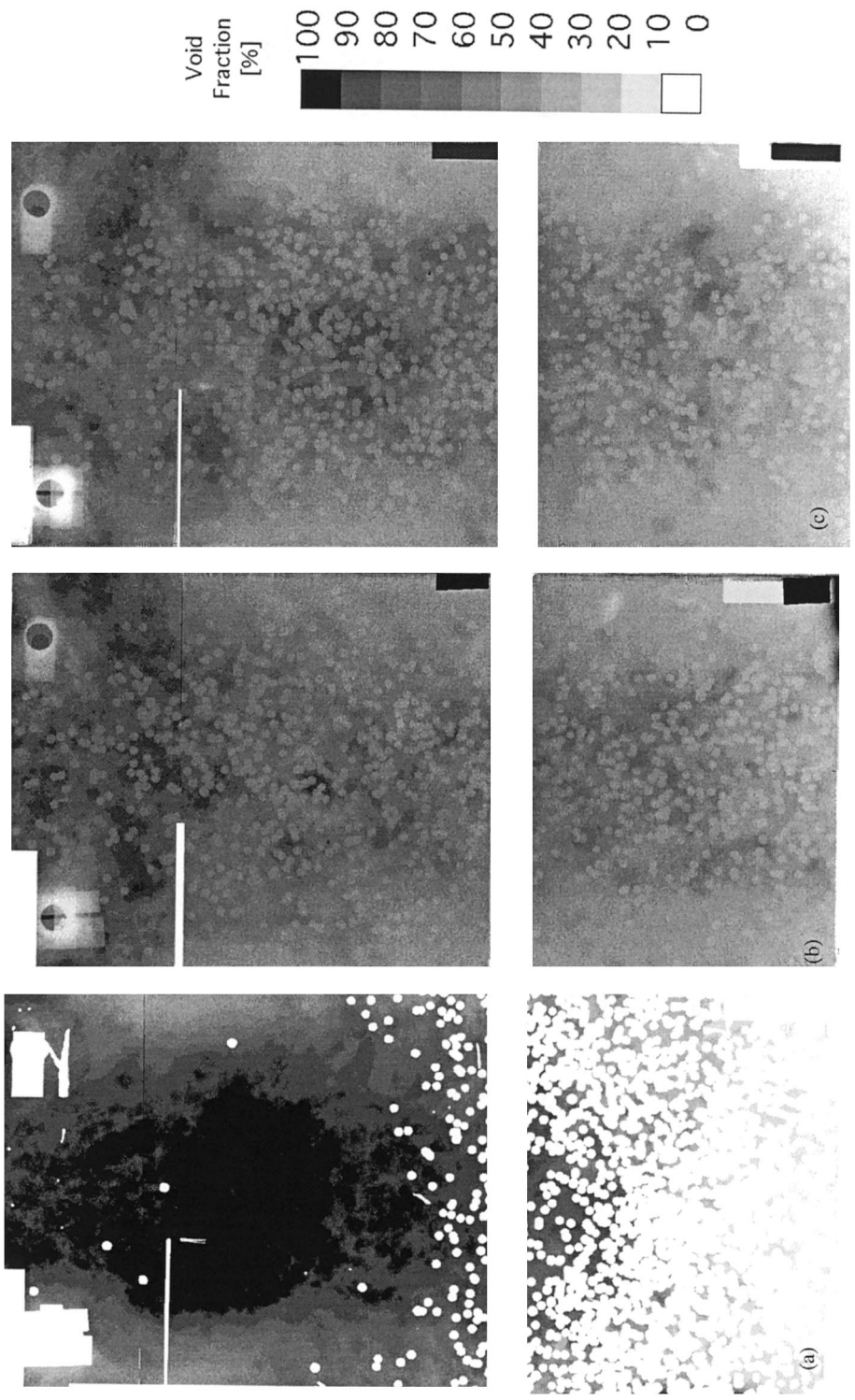

Fig. 12. Quantified images of selected radiographs in Fig. 11. The (a), (b), and (c) correspond to runs 13, 14, and 16 in Table 2. The void fraction scale is to be applied everywhere outside the particle locations, and this is done as part of the data analysis, which, as a first step, involves identification of all particles, as shown in white in (a).

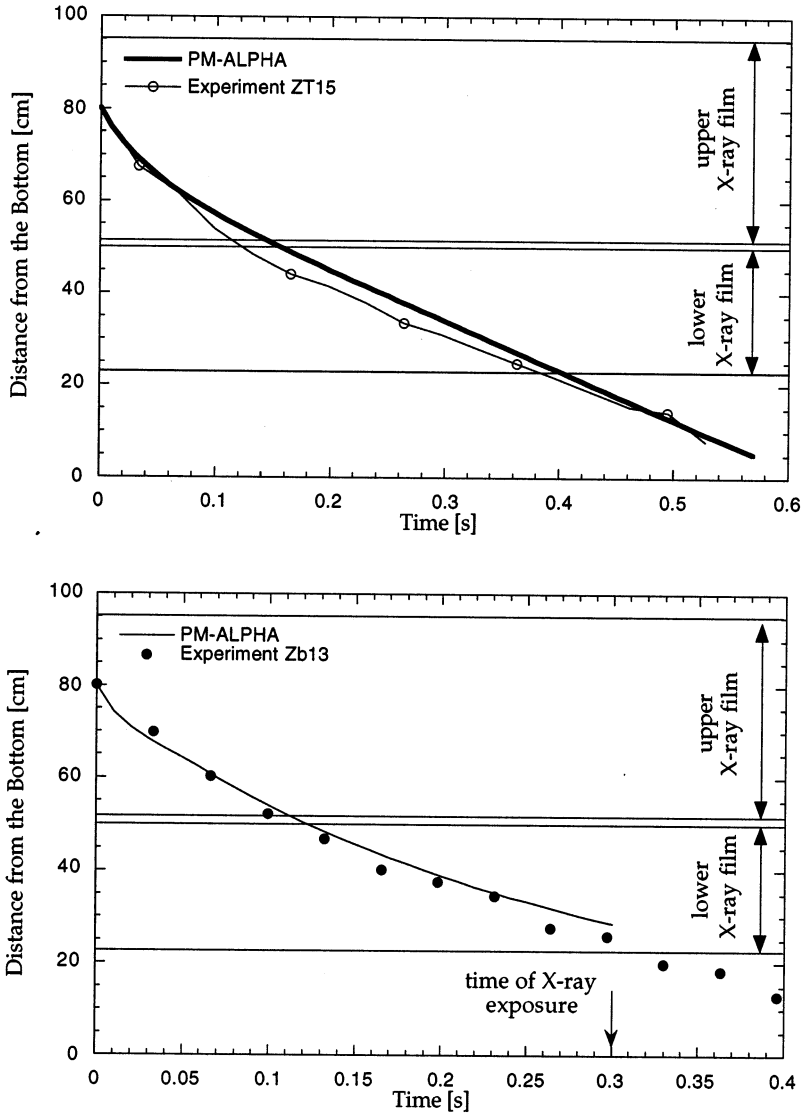

Fig. 13. Front advancement in two hot runs at 0.5% (top) and 5.5% (bottom) inlet particle volume fractions, and typical comparisons with PM-ALPHA predictions. Also shown are the regions covered by the two X-ray cassettes.

conditions be completely characterized, so as to avoid any empirical factors from entering such comparisons. In particular, this means uniform and precisely known temperatures for both the particulate and the liquid pools, uniformity of particle cloud, and precise knowledge of the solids concentration and velocity, at some point prior to the plunge. Because of the significant role of phase change, which with subcooled pools involves also condensation, the volume fraction distributions of the three constituents, particles, liquid, and vapor, are of principal interest. The evolution with time of such constituent 'maps' characterize completely the interactions. With precisely controlled conditions these time evolutions can be constructed from single flash X-ray shots at varying time delays, in repeat experiments. Reproducibility is confirmed by duplicate runs,

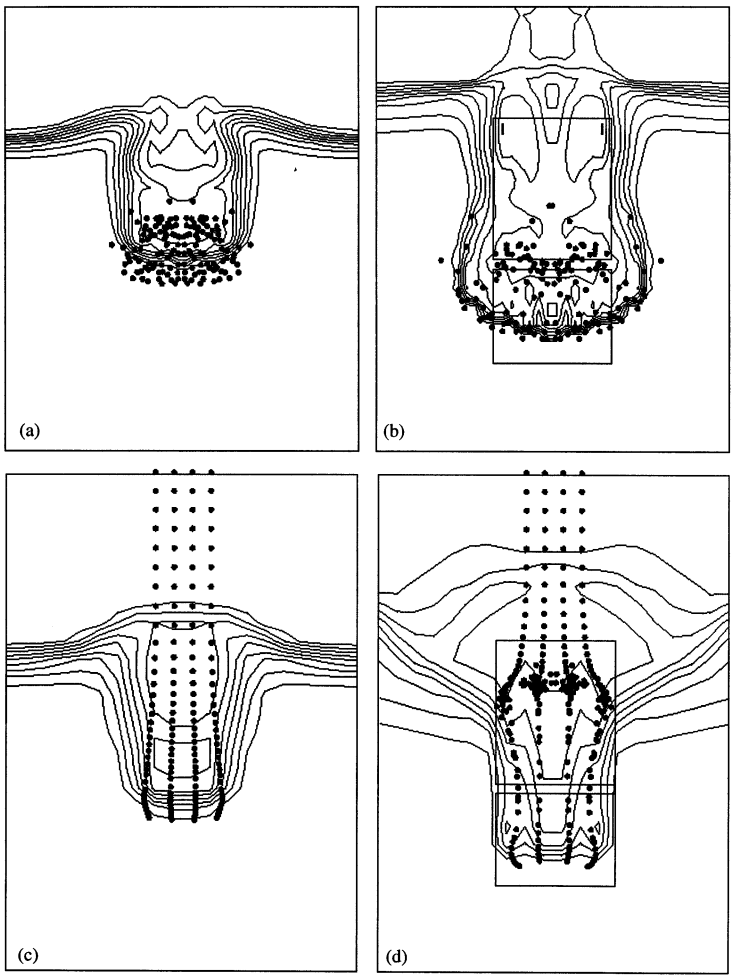

Fig. 14. PM-ALPHA predictions for runs Zb13 (a, b), and ZT15 (c, d). The times are (0.15, 0.3) and (0.5, 0.8) s, respectively. The (b) and (d) images correspond to the time of X-ray shots. The X-ray film outline is also shown. The particles are Lagrangian and projected volume fractions agree well with the measurements. The void fraction contours go from 0.1 to 0.9 in increments of 0.1. Note the densification occurring at the front due to particle deceleration, and the resuspension occurring due to the intense counter-current flow at latter times.

and also by external, overall observations from two video cameras that record every interaction.

An overall schematic of MAGICO is shown in Fig. 3. The key component of the furnace is a heating element, constructed from a graphite block, as shown in Fig. 4. Using ZrO_2 particles, masses of up to ~ 6 kg can be accommodated within the cylindrical channels shown. A special mechanism involving tungsten doors is used to create a sudden and 'clean' release. A special device is placed below the furnace, if a further dilution (to lower concentrations) of the cloud is desired. The test section used in the experiments discussed here is shown in Fig. 5. With it, we obtain a cleanly two-dimensional (Cartesian) behavior, and hence the most direct interpretation of the radiographs. Details of MAGICO and of the main problem that motivated it can be found in Theofanous et al. (1996a).

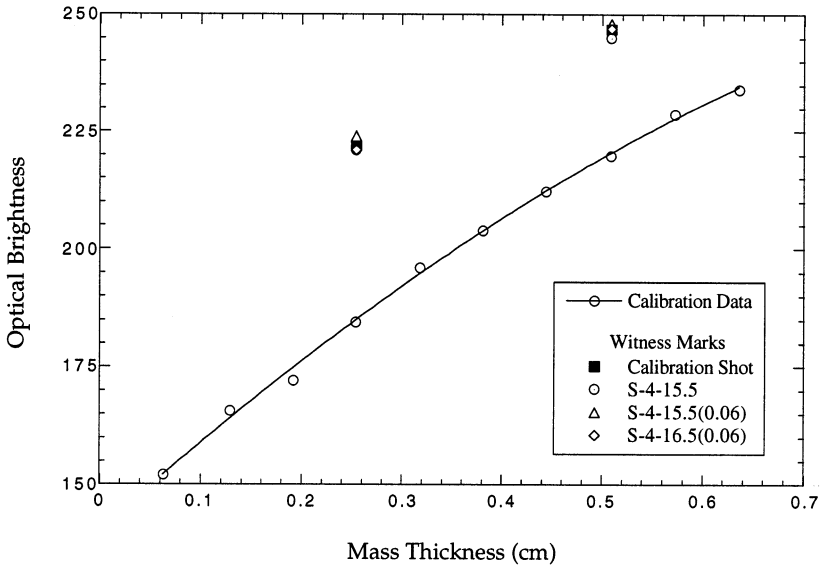

Fig. 15. Calibration for iron in SIGMA, and witness marks in various runs.

Table 3
Conditions and timing for the SIGMA runs

Steel runs Pressure: 27.2 Mpa		Void fraction: 0 or 6%	Temperature: 1550 and 1650°C*	
	S4-15.5(0)	S4-15.5(0)	S4-15.5(0.06)	S4-16.5(0.06)*
Time (ms)	0	0.32	0.12	0.22
Steel runs Pressure: 27.2 Mpa		Void fraction: 6%	Isothermal at room temperature	
	Ga4-0	Ga4-6a	Ga4-6b	Ga4-6c
Time (ms)	0	0.30	0.46	0.74

3.2. Illustrative results and discussion

A typical calibration curve is shown in Fig. 6. The kind of variability obtained is illustrated in Fig. 7. This figure shows also the 'witness pieces' and how well they, by themselves, reflect the variability between shots. Finally, Fig. 8 provides an illustration of how the calibration curve is applied to an experimental run, through the slight shift suggested by the 'witness' readings. For these measurements we estimate an error of less than 5%.

The two groups of experiments from which illustrative results are reported here are summarized in Tables 1 and 2. The cold runs were conducted with both particulate and water at room temperature. The numerical simulations referred to below were carried out with the computer code PM-ALPHA (Theofanous et al., 1996a).

The sequence of shots in the ZCN runs, in Fig. 9, show, in fascinating detail, an interesting cavity opening and closing phenomenon behind the plunging cloud. At the other extreme, for the conditions of the ZCT runs, the pool surface remains relatively undisturbed, as illustrated in Fig. 10. Only a relatively small amount of gas is entrained by individual particles in this case.

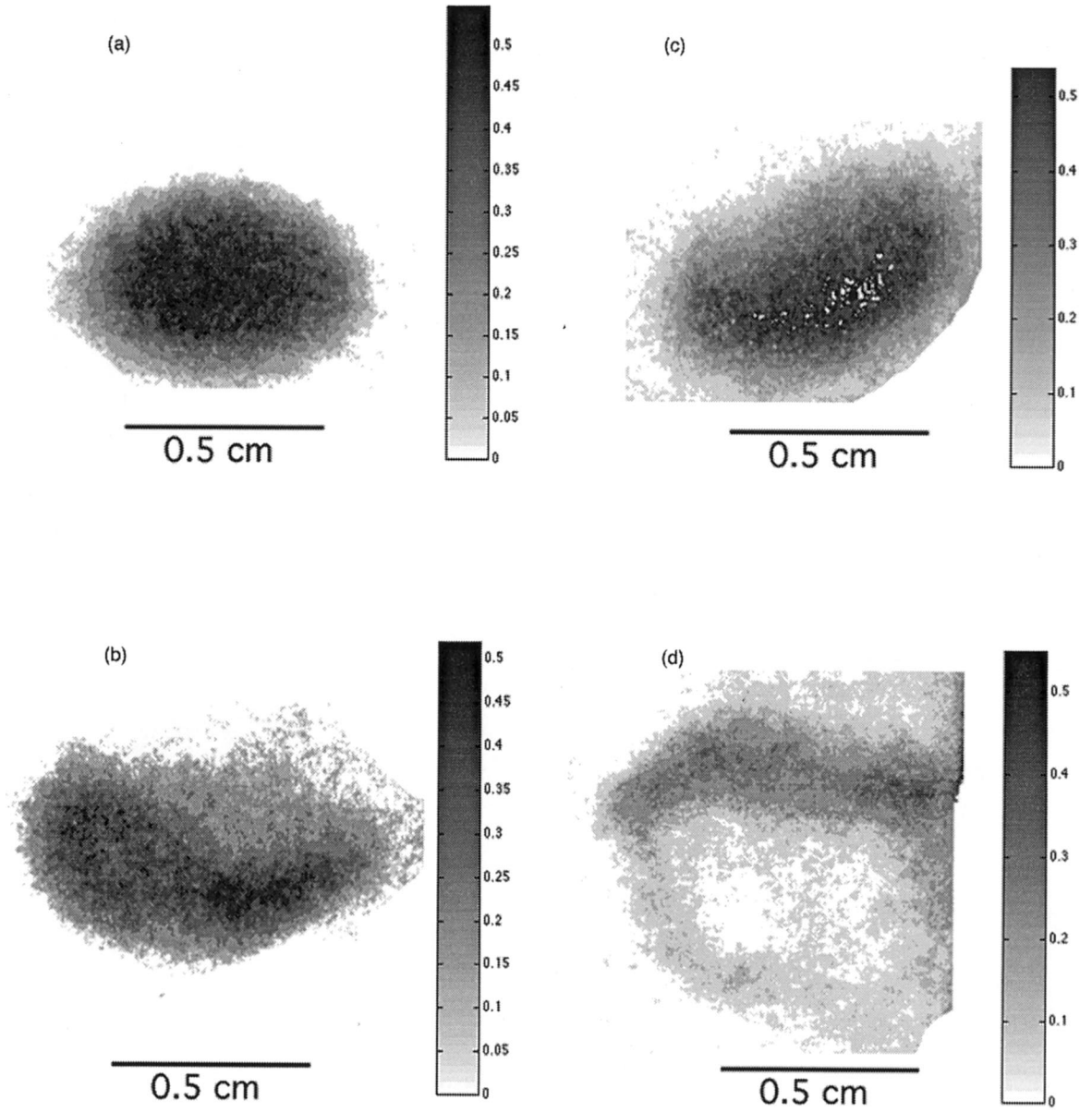

Fig. 16. Reconstruction of X-ray images from the SIGMA iron runs in Table 3. The (a), (b), (c), and (d) correspond to 0, 0.32, 0.12, and 0.22 shot times.

Clearly, the former situation is dominated by inertia effects. The latter one, with hot particles, on the other hand, gives rise to a predominantly thermal interaction regime, as described below. With experiments and computations well anchored in these two extremes, the more complex intermediate regimes can be approached with some sense of overall perspective for completeness.

The radiographs from the six hot runs are shown in Fig. 11. Quantified void fraction maps from three runs with large particles are collected in Fig. 12. Two front trajectories, with corresponding predictions, are shown in Fig. 13. We

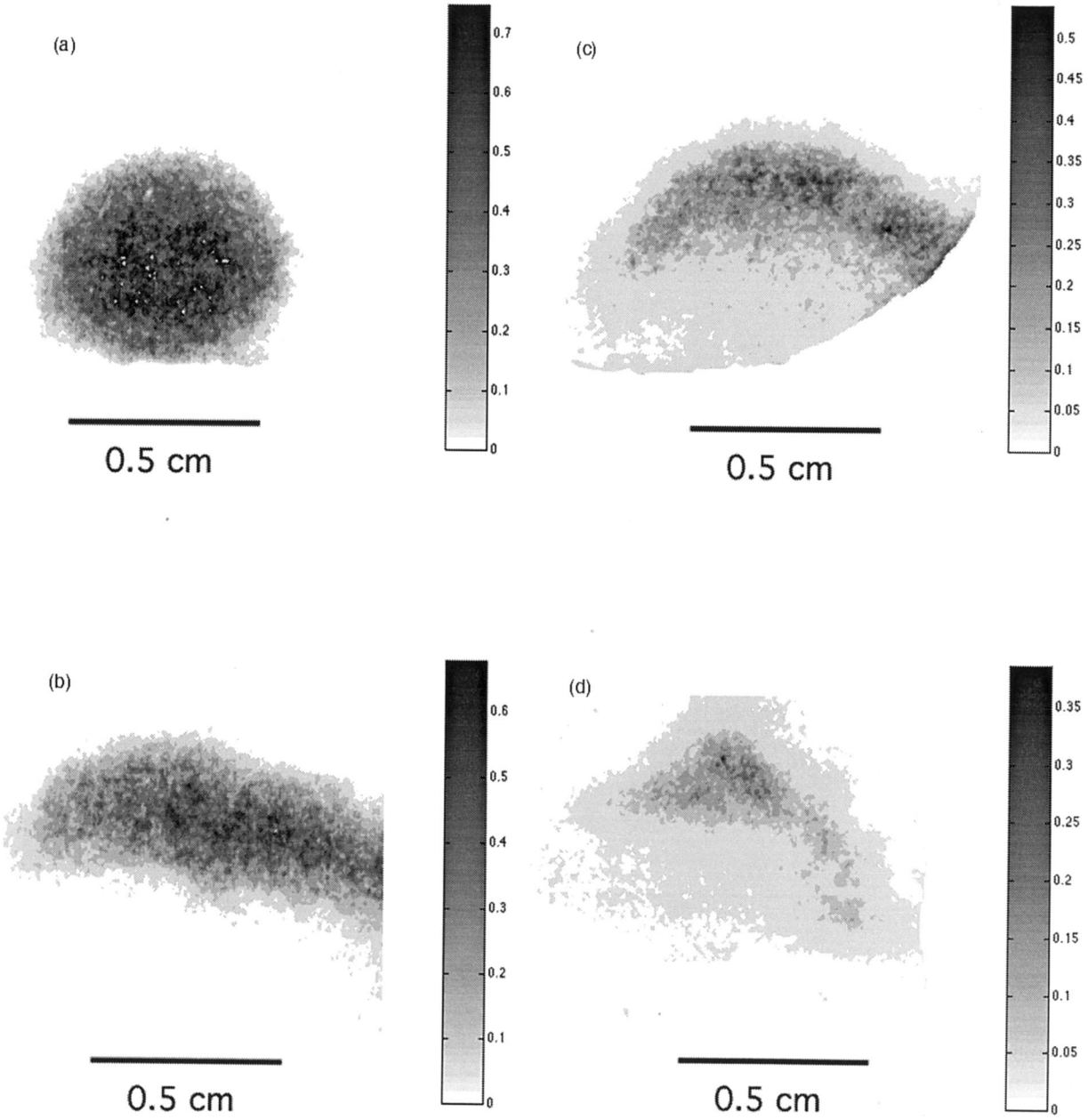

Fig. 17. Reconstruction of X-ray images from the SIGMA gallium runs in Table 3. The (a), (b), (c), and (d) correspond to 0, 0.30, 0.46, and 0.74 shot times.

find that by reducing the particle concentration from 5.5 to 0.5% the penetration time is reduced by $\sim 25\%$. It is also interesting to note that the dilute cloud reaches terminal velocity rather quickly, but for the denser cloud this is far from being the case all the way to the end. Further, in Figs. 11 and 12, the following observations can be made.

- Between 11(a) and (b) we can discern the important influence of 10°C subcooling on the

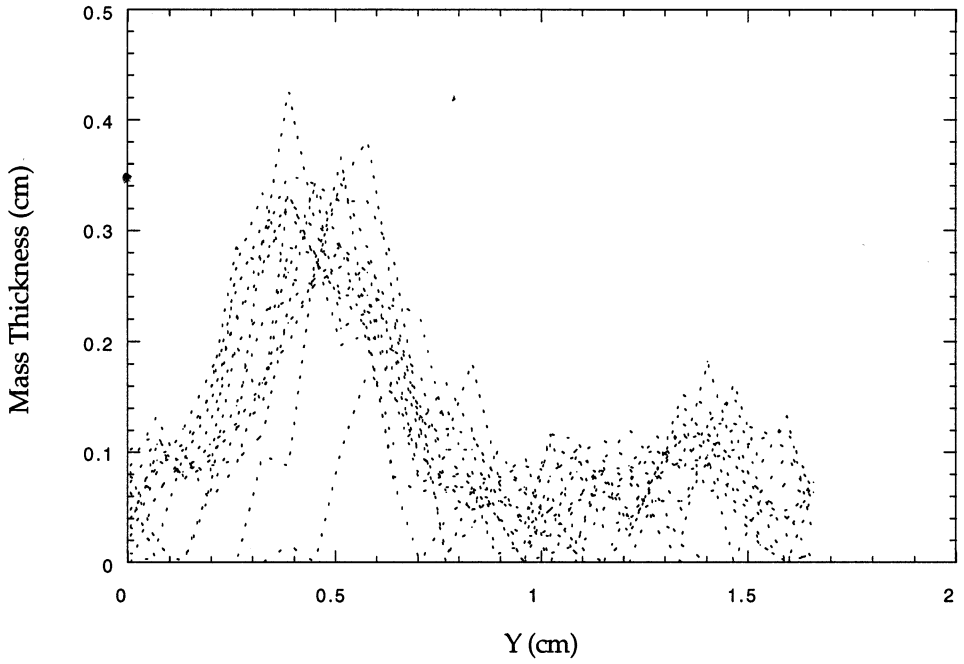

Fig. 18. Illustration of mass thickness distribution along slices through the radiographic image of run S4-16.5(0.06).

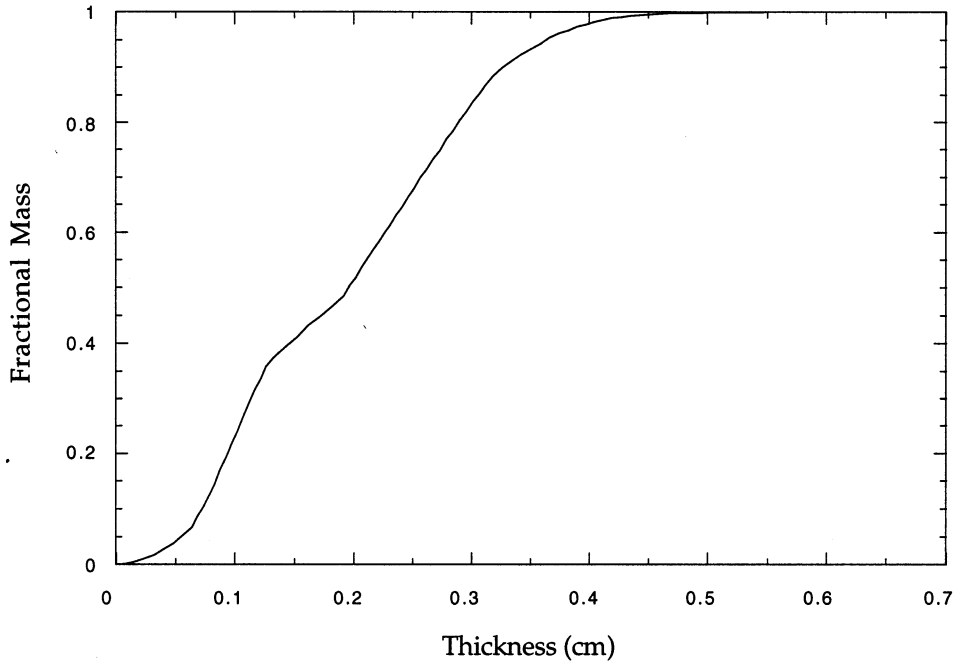

Fig. 19. Cumulative mass distributions computed from the results of Fig. 18.

boundaries of the highly voided (nearly 100%) portion of the mixing region. Also interesting is the contrast between these two and the cold runs of Fig. 9.

- Between 11(c) and (e) (12(a) and (b)) we can observe the essential difference between the inertia and thermal regimes, mentioned above. Also interesting to note is the intricate structure of the two-phase region in 11 (c).
- Finally, between 11(d), (e) and (f) (12(b) and (c)) we can capture the increasing voiding obtained as the particulate temperature increases from 1650 to 2000°C.

The utility of these data in terms of CFD results is illustrated by the PM-ALPHA simulations shown in Fig. 14. These were conducted for runs Zb13 and ZT15 of Table 2, the main difference between them being the inlet particulate concentration (which as described above leads to a major difference in interaction regimes). The evaluation of the pattern is important in such comparisons, and the unique power of this measurement technique in this respect is quite evident. In particular, note the highly voided portion in the upper part of Fig. 14(b), as in Fig. 12(a), and the quantitative void pattern comparison between Figs. 14(d) and 12(b). Also, the particle volume fractions agree quantitatively, and so is the resuspension shown in Fig. 14(d).

4. Application to microinteractions in large-scale steam explosions

4.1. The SIGMA facility

The SIGMA facility is a hydrodynamic shock tube, capable of delivering ~ 2 ms duration shocks, of amplitude up to 100 MPa (15000 psi). A small (~ 1 g) quantity of a high-temperature melt is generated and released by a special device, inside the shock tube, and it is forced to interact (actually explode) with the surrounding water, by the shock wave, coming from above. The process is timed so that the interaction occurs within the view of a window, through which a high-speed movie (50000 frames per second), and a single flash X-ray shot, are obtained simultaneously. The timing of the X-ray shot is controlled so as to obtain the evolution in repeat runs, as done for the experiments discussed in the previous section. The difference here is that the time frame is in 100s of microseconds, and the spatial scale is much smaller as well. Both the coolant velocity and pressure level behind the shock are important here, and experimentally, various combinations can be achieved by selecting the initial pressure level in the driver, and the void fraction in the coolant column (by embedding appropriately supported quantities of small gas bubbles, contained in thin plastic). It is thus possible to experimentally simulate large-scale steam explosions at the microscopic level, and in a manner that lends itself to detailed quantification of the finescale fragmentation and consequent micromixing (termed microinteractions), both of which are the principal mechanisms of the explosion. These quantifications, in turn, are used for the development of appropriate constitutive laws, and ultimately for the a priori prediction of the explosion wave dynamics (Theofanous et al., 1996b). This reference contains also the details of the SIGMA facility.

4.2. Illustrative results and discussion

Here, calibrations are obtained by placing a stepwedge, made of the same material to be used as the melt, in the area of the window. Again, we use witness pieces, in the manner described above. A typical calibration curve, and the reproducibility of the witness marks in actual experiments are illustrated in Fig. 15. Another indication of precision can be obtained by comparing the calculated masses, from image analysis, to the known masses of the drops. For the four iron-drop cases discussed below, we found 0.98, 0.98, 1.10, and 1.06, as compared to the 1 g quantity placed in the melt generator. Separate tests with thin layers of recovered debris indicate that the limit of detection in the present arrangement is ~ 0.2 mm. The two groups of runs reported here are specified in Table 3. Coolant speeds of ~ 20 and 40 m s^{-1} are obtained with 0 and 6% voids, respectively.

The reconstructed images from the radiographs are shown in Figs. 16 and 17. The data analysis

currently takes the form illustrated in Figs. 18 and 19. From these, in conjunction with the reconstructed images, one can determine the degree of fragmentation and the degree of mixing with the coolant in the vicinity. These, in turn, are used in conjunction with numerical simulations (Theofanous et al., 1996b) to test models and further develop models and correlations. With reference to Figs. 16 and 17, it is especially interesting to note the great differences in the patterns of fragmentation and mixing between the isothermal gallium and the high-temperature iron drops.

5. Conclusions

By special attention to experimental technique, delivery of the X-ray pulse, and film development and calibration procedures, radiographic images of complex multidimensional, multiphase flows can be quantitatively interpreted. The technique offers unique advantages, in allowing access to the internal flow structure and its evolution with time. This is an important modern need, as the confluence of multifield modelling and computational advances create the opportunity for the detailed prediction of such flows.

References

Brown, J.G., 1966. X-Rays and their Applications. Plenum Press, New York, New York.

Harvel, G.D., Hori, K., Kawanishi, K., Chang, J.S., 1996. Real-time cross sectional averaged void fraction measurements in vertical annulus gas-liquid two-phase flow by neutron radiography and X-ray tomography techniques. Nucl. Instrum. Methods Phys. Res. A 371, 544–552.

Mishima, K., Hibiki, T., 1997. Development of high-frame rate neutron radiography and quantitative measurement method for multiphase flow research. OECD/CSNI Specialist Meeting on Advanced Instrumentation and Measurement Techniques, Santa Barbara, CA.

Narabayashi, T., Tobimatsu, T., Nagasaka, H., Kagawa, T., 1984. Measurement of transient flow pattern by high speed scanning X-ray void fraction meter. In: Delhaye, J.M., Cognet, G. (Eds.), Measuring Techniques in Gas–Liquid Two-Phase Flows, IUTAM Symposium Nancy 1983. Springer-Verlag, Berlin, pp. 259–280.

Smith, A.V., 1971. Transient density measurements in two-phase flows using X-rays. J. Br. Nucl. Eng. Soc. 10, 99–106.

Theofanous, T.G., Yuen, W.W., Angelini, A., 1996a. Premixing of steam explosions: PM-ALPHA verification studies. Technical report DOE/ID-10504, US Department of Energy.

Theofanous, T.G., Yuen, W.W., Freeman, K., Chen, X., 1996b. Propagation of steam explosions: ESPROSE.m verification studies. Technical report DOE/ID-10503, US Department of Energy.

Zavaglia, J.C., Lindsay, J.D., 1989. Flash X-ray visualization of multiphase flow during impulse drying. Tappi J. 72, 79–85.